A dynamic state observer for real-time reconstruction of the tokamak plasma profile state and disturbances

Federico Felici[1], Marco de Baar[1,2] and Maarten Steinbuch[1]

Abstract— A dynamic observer is presented which can reconstruct the internal state of a tokamak fusion plasma, consisting of the spatial distribution of current and temperature, from measurements. Today, the internal plasma state is usually reconstructed by solving an ill-conditioned inversion problem using a large number of measurements at one point in time. Such an approach does not take into account the time evolution of the underlying dynamical system (the plasma) and strongly relies on (technically challenging) internal measurements. The observer-based approach presented here includes the dynamics of the plasma current and temperature, modeled by a set of coupled nonlinear 1-D PDEs which are discretized in space and time to yield a finite-dimensional nonlinear model. The observer, which is based on an Extended Kalman Filter, estimates the state of an augmented model which includes additive state disturbances modeled as a random walk. Simulation results demonstrate the effectiveness of this observer in the case of perturbed models and input disturbances.

I. INTRODUCTION

The tokamak, a type of magnetic plasma confinement device, is at present one of the more promising candidates for reaching controlled thermonuclear fusion for electricity production (see [1], [2] for a control-oriented introduction). In a tokamak, the axisymmetric magnetic fields which confine the plasma are generated by a combination of electrical currents in external coils and in the plasma itself. Plasma control is a key element of tokamak operations, and has expanded in recent years from control of bulk plasma quantities (position, total plasma current and volume-integrated pressure) to control of the spatial distribution of the pressure and current density profile. Actuators for pressure and current profile tailoring include inductive voltage from the primary tokamak transformer coil, as well as auxiliary heating and current drive effected by a combination of radiofrequency or neutral particle sources.

For real-time control purposes, but also for performance and safety monitoring, it is crucial to know in real-time the internal distribution of electrical current as well as temperatures and densities of plasma electrons and ions. These quantities are approximately constant on nested "flux" surfaces on which magnetic field lines lie (Fig.1), and can be represented as functions of the variable ρ (a metric for the radial distance from the magnetic axis). They are measured by a set of complex plasma diagnostic systems, [3]. External magnetic fields and currents can readily be measured outside
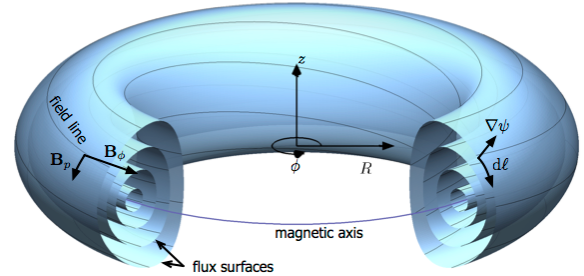
[1] Eindhoven University of Technology, Faculty of Mechanical Engineering, Control Systems Technology group. P.O. Box 513, 5600 MB Eindhoven, The Netherlands. f.felici@tue.nl
[2] FOM-Institute DIFFER - Dutch Institute for Fundamental Energy Research, PO Box 1207, 3430 BE Nieuwegein, The Netherlands.

Fig. 1. Schematic representation of flux surfaces of a tokamak plasma. (R, ϕ, z) is a cylindrical coordinate system around the vertical axis z. B_p is the magnetic field in the "poloidal" Rz plane. B_ϕ is the magnetic field in the "toroidal" ϕ direction. These fields are orthogonal to the gradient $\nabla \psi$ of the poloidal flux $\psi(R, Z) = \iint_{S_z} \mathbf{B} \cdot \mathbf{dS_z}$, with S_z a horizontal disk bounded by (R, Z).

the plasma, while internal plasma quantities (temperature, density, internal currents and fields) must be measured remotely as it is not possible to place any measurement equipment inside the plasma. All these measurements must then be combined into one self-consistent estimate for the plasma state at a given time. Traditionally, this is done by parametrizing the 1D profiles (as a function of ρ) as a sum of a small number of basis functions, thereby reducing the dimensionality of the problem, and then numerically solving a 2D nonlinear elliptic partial differential equation representing the plasma Magneto-Hydrodynamic force balance, while seeking basis function parameters minimizing some least-squares criterium on the measurements. This procedure is known as (real-time) constrained equilibrium reconstruction and is routinely performed in many tokamaks [4], [5].

In most situations, existing techniques provide satisfactory estimates of the position and boundary of the plasma, but have difficulty in accurately reconstructing the internal current density distribution near the plasma core since details of the spatial structure of the internal current density distributions are shielded from external magnetic measurements [5]. Internal measurements are necessary, but these are technologically very difficult and not always available or reliable. When they are available, the number of basis functions used in the representation of the internal profiles is still constrained by the number of measurement points. However, accurate knowledge of the core current distribution is of crucial importance for plasma stability and quality of thermal confinement.

Recent contributions on feedback control of the plasma profiles [6], [7], [8], [9] have explored controllers based

on models of the plasma profile dynamics (derived from physical laws or identified from data). All these approaches assume the to-be-controlled quantities to be known, but as outlined above this is usually not straightforward. In this paper we therefore design a model-based observer with the aim of providing better estimates of these internal quantities, in particular for feedback control.

Model-based observer design for plasma profile reconstruction has received comparably little attention. Previous work by other authors, most notably [10], started to address the problem by using an Extended Kalman Filter (EKF) for estimating the transport parameters of a single 1D PDE for thermal transport based on temperature measurements. More recent work [11] addresses the same problem, again focusing on the temperature profile but assuming that the inputs are also unknown.

In this work we address the problem of simultaneously estimating the electron temperature and current density profile, whose evolution is dynamically coupled, using a combination of several measurements of different physical quantities. We design an Extended Kalman Filter (EKF) [12] which employs a nonlinear model for the time evolution of the state, and linearizations of the nonlinear model for the state measurement update and covariance equations. It is assumed that the model parameters are known, and model or parameter errors are interpreted as additive disturbances in the state equation, which are estimated by the EKF. We argue that this is more appropriate for implementation on an operational tokamak than on-line parameter estimation, as this introduces additional nonlinearity into the problem which might make the filter behaviour unpredictable. Also, adapting the model parameters makes it more difficult to distinguish in real-time between modeling errors and sudden faults, while disturbance estimation allows for a more straightforward interpretation of the plant-model mismatch. The real-time estimated disturbances can be analyzed and classified as (normal) noise or modeling errors, or as (off-normal) sensor, actuator or process faults.

The inclusion of a realistic plasma model in the observer is enabled by the RAPTOR code [13], [14] which is capable of evolving a nonlinear model of the plasma profile dynamics in real-time, which means $< 5\text{ms}$ on most tokamaks, while returning analytically computed local linearizations at each time step.

The remainder of this paper is structured as follows. Section II briefly introduces the tokamak transport model describing the process and provides information about the numerical code used to simulate the model. Section III analyzes the observability of the system and describes the design of the EKF. Section IV investigates the observer performance using simulations, including several types of simulated disturbances as well as realistic sensor noise conditions and modeling errors. Finally Section V summarizes the results and points towards future research.

II. MODEL DESCRIPTION

A. Model derivation

Transport in a tokamak is modeled by the combination of a set of 1D partial differential equations for radial transport and a 2D elliptical PDE for the plasma magnetic equilibrium. A complete treatment is beyond the scope of this paper, but one may refer to [15] or [16] for details. Physics-oriented simulators for tokamak plasmas exist (e.g. [17], [18], [16]) but these are not well suited for controller/observer design. Simplified, control-oriented models have appeared in recent literature, ranging from identified linear models around equilibrium points [6] to more complete, nonlinear models [19], [20], [21], [7] including, more recently, the model contained in the real-time RAPTOR code [13],[14]. The physics model solved in RAPTOR will be discussed in the remainder of this section.

An approximate model of 1D tokamak transport is obtained by simulating the response of physical quantities $\psi(\rho,t)$ (poloidal magnetic flux) and $T_e(\rho,t)$ (electron temperature) to the available actuators, where all other quantities (2D equilibrium, density, ion temperature) are kept constant. The coupled evolution of these two quantities contains the key nonlinearities of the process.

These equations for the simultaneous evolution of ψ and T_e can be written as two coupled, nonlinear parabolic PDEs on $\Omega = \{t \in \mathbb{R},\ \rho \in \mathbb{R}\ |\ t_0 \le t \le t_f,\ 0 \le \rho \le 1\}$. (details of the derivation can be found in [14] and [22])

$$m_\psi(T_e)\frac{\partial \psi}{\partial t} = \frac{\partial}{\partial \rho}\left(d_\psi \frac{\partial \psi}{\partial \rho}\right) + f_\psi(\psi, T_e)$$
$$+ \sum_{i=1}^{m-1} S_{i,\psi}(T_e)P_i(t) \qquad (1)$$

$$m_{T_e}\frac{\partial T_e}{\partial t} = \frac{\partial}{\partial \rho}\left(d_{T_e}(\psi, T_e)\frac{\partial T_e}{\partial \rho}\right) + f_{T_e}(\psi, \frac{\partial \psi}{\partial t})$$
$$+ \sum_{i=1}^{m-1} S_{i,T_e}P_i(t) \qquad (2)$$

On the right-hand side of both equations we find the actuator input powers $P_i(t) \in \mathbb{R}_0^+$. All other quantities depend on the spatial variable ρ and (nonlinear) dependencies on ψ or T_e are explicitly mentioned. For a complete listing of the various expressions the reader can refer to [14], but for completeness we list the main nonlinear dependencies here: $m_\psi(T_e) \sim \rho T_e^{3/2}$, $f_\psi(\psi, T_e) \sim \partial T_e/\partial \psi$ $S_{i,\psi}(T_e) \sim T_e$, $f_{T_e} \sim \frac{\partial^2 \psi}{\partial \rho^2} \cdot \frac{\partial \psi}{\partial t}$, $d_{T_e}(\psi, T_e) \sim \rho^2 \partial \rho/\partial \psi F(s)$ where $F(s) = (1 + \exp(k - s))^{-1}$, $s \sim (1 - \rho \frac{\partial \rho}{\partial \psi}\frac{\partial^2 \psi}{\partial \rho^2})$ and k is a constant. The last equation represents an empirical model of the change in thermal transport due to local magnetic field gradients, which approximates a markedly more complicated physical dependence involving plasma turbulence. An important feature of this model is that for low magnetic shear s the local thermal diffusivity is reduced.

The boundary conditions are $\frac{\partial \psi}{\partial \rho}(0) = 0$, $\frac{\partial T_e}{\partial \rho}(0) = 0$ (due to the cylindrical coordinate system used) and $\frac{\partial \psi}{\partial \rho}(1) = c_{I_p}I_p(t)$, $T_e(1) = T_{eb}$, where $I_p(t)$ is the plasma current and

T_{eb} is the edge temperature (c_{I_p} is a constant). The first is included as input to the model, while the second is chosen as a parameter.

Sensors (plasma diagnostics) are modeled as a nonlinear equation, assumed smooth and continuously differentiable:

$$y_k = h(x_k) \qquad (3)$$

B. Numerical simulation including first order sensitivities

Solving the coupled PDEs is not a trivial problem, particularly since the equations are stiff due to the high sensitivity of the thermal transport to the second derivative of the flux profile. The numerical scheme used to discretize and solve the problem is discussed below.

The equations are discretized in space by the Finite Element method. Flux and temperature profiles are written as

$$\psi(\rho, t) = \sum_{\alpha=1}^{n_{sp}} \Lambda_\alpha(\rho) \hat{\psi}_\alpha(t), \qquad (4)$$

$$T_e(\rho, t) = \sum_{\alpha=1}^{n_{sp}} \Lambda_\alpha(\rho) \hat{T}_{e\alpha}(t), \qquad (5)$$

where as Λ_α we choose n_{sp} cubic B-splines [23] with a finite support, and $\hat{\psi}$ and $\hat{T}_e$ are the time-varying spline coefficients which will represent the state of our system. The basis function set is chosen so as to identically satisfy the boundary conditions at $\rho = 0$. Projecting the equation onto the finite elements yields a weak form, which reduces the set of PDEs above to a set of nonlinear matrix ODEs involving $\hat{\boldsymbol{\psi}} = [\hat{\psi}_1, \ldots, \hat{\psi}_{n_{sp}}]^T$ and $\hat{\mathbf{T}}_e = [\hat{T}_{e1}, \ldots, \hat{T}_{en_{sp}}]^T$.

$$0 = -\mathbf{M}_\psi(\hat{\mathbf{T}}_e)\dot{\hat{\boldsymbol{\psi}}} - \mathbf{D}_\psi\hat{\boldsymbol{\psi}} + \mathbf{s}_\psi(\hat{\boldsymbol{\psi}}, \hat{\mathbf{T}}_e, \mathbf{u}) \qquad (6)$$

$$0 = -\mathbf{M}_{T_e}\dot{\hat{\mathbf{T}}}_e - \mathbf{D}_{T_e}(\hat{\boldsymbol{\psi}}, \hat{\mathbf{T}}_e)\hat{\mathbf{T}}_e + \mathbf{s}_{T_e}(\hat{\boldsymbol{\psi}}, \dot{\hat{\boldsymbol{\psi}}}, \hat{\mathbf{T}}_e, \mathbf{u}) \quad (7)$$

Where $\hat{\boldsymbol{\psi}}, \hat{\mathbf{T}}_e, \mathbf{s}_\psi, \mathbf{s}_{T_e} \in \mathbb{R}^{n_{sp}}$, $\mathbf{M}_\psi, \mathbf{D}_\psi, \mathbf{M}_{T_e}, \mathbf{D}_{T_e} \in \mathbb{R}^{n_{sp} \times n_{sp}}$. The edge boundary condition for ψ is explicitly included in the input vector, such that

$$\mathbf{u} = [I_p, P_1, P_2, \ldots, P_m]^T \in \mathbb{R}^m. \qquad (8)$$

We define the state as

$$x(t) = \begin{bmatrix} \hat{\boldsymbol{\psi}}(t) \\ \hat{\mathbf{T}}_e(t) \end{bmatrix} \in \mathbb{R}^{n_x} \qquad (9)$$

and define, for later convenience, selection matrices $\mathbb{S}_\psi$ and $\mathbb{S}_{T_e}$ such that $\hat{\boldsymbol{\psi}}(t) = \mathbb{S}_\psi x(t)$ and $\hat{\mathbf{T}}_\mathbf{e}(t) = \mathbb{S}_{T_e} x(t)$.

We choose a first-order discretization of the time derivative $\dot{x}(t_k) = (x_{k+1} - x_k)/\Delta t$, $x(t_k) = \theta x_{k+1} + (1 - \theta)x_k$ and $u(t_k) = u_k$. In practice, $\theta = 1$ is used for stability reasons. The equations are solved in time using a fully implicit nonlinear scheme. Combining equations (6), (7) into the implicit expression

$$\hat{f}(\dot{x}(t), x(t), u(t), t) = 0. \qquad (10)$$

we can then rewrite the discrete-time equivalent of (10) as

$$\tilde{f}_k \equiv \tilde{f}(x_{k+1}, x_k, u_k) = 0 \quad \forall\, k \qquad (11)$$

The state at the next time step x_{k+1} is computed at each time step by Newton iterations, terminating the iterations if the residual $\|\tilde{f}_k\| < \epsilon$ with very small ϵ. As is often the case when numerically solving nonlinear equations, care must be taken to initialize the iterations close to a valid solution and to choose an appropriate time step and residual tolerance. Benchmarks of RAPTOR versus the more complete transport code ASTRA [16] and CRONOS [18], have confirmed the numerical accuracy of the code.

The Jacobians $\partial \tilde{f}/\partial x_{k+1}$, $\partial \tilde{f}/\partial x_k$ and $\partial \tilde{f}/\partial u_k$, are analytically evaluated at every time step by copious application of the chain rule. Once these Jacobians are known, the linearization of the nonlinear model around the nominal nonlinear trajectory (x_k^o, u_k^o) is readily computed as

$$\tilde{x}_{k+1} = A_k \tilde{x}_k + B_k^u \tilde{u}_k \qquad (12)$$

$$\tilde{y}_k = C_k \tilde{x}_k \qquad (13)$$

where $\tilde{x}_k = x_k - x_k^o$ and $\tilde{u}_k = u_k - u_k^o$.

$$A_k = -\left(\frac{\partial \tilde{f}}{\partial x_{k+1}}\right)^{-1} \frac{\partial \tilde{f}}{\partial x_k}, \qquad (14)$$

$$B_k^u = -\left(\frac{\partial \tilde{f}}{\partial x_{k+1}}\right)^{-1} \frac{\partial \tilde{f}}{\partial u_k}, \qquad (15)$$

$$C_k = \left.\frac{\partial h}{\partial \tilde{x}_k}\right|_{x_k^o} \qquad (16)$$

where the Jacobians are evaluted at (x_k^o, u_k^o). The Jacobian $(\partial f/\partial x_{k+1})$ is invertible along typical state trajectories.

The RAPTOR code, implemented in MATLAB, takes < 5 milliseconds per time step with 34 states on a Quad-Core Intel®Core™i5-2500 CPU at 3.3GHz PC running Linux. This allows a simulation of a full tokamak discharge to be completed in a few seconds, representing a marked improvement over more complex physics-oriented codes, which may take several minutes or hours to do the same. As such, RAPTOR represents a very useful tool for use as a real-time observer, in real-time predictive schemes, but also for control-oriented plasma simulations used for controller benchmarking.

C. Sensors

For this paper, we will assume a standard set of sensors (called *diagnostics* in the plasma physics field) available on most advanced tokamaks. They are listed Table I including the typical standard deviation of each measurement, representative for the technical capabilities of plasma diagnostics. These standard deviations are used in the remainder of this paper to generate artificial noise to corrupt the measurements used in the state reconstruction. Note that while the electron temperature T_e is measured directly, only the edge value of the poloidal flux ψ (at $\rho = 1$) is measured and only other information about the spatial derivative of ψ is available at other ρ locations through the quantity $\iota = \frac{1}{2\pi B_0 \rho}\frac{\partial \psi}{\partial \rho}$. In reality, ι is also not measured directly but can be obtained from internal current profile diagnostics via a transformation which we will not discuss here.

Symbol	Unit	σ of error	Description	Measurement type	Typical diagnostic
ψ_b	Wb	1mWb	Poloidal flux on plasma edge	Scalar	Equilibrium reconstruction
I_p	kA	1kA	Total plasma current	Scalar	Magnetic sensors
T_e	keV	100eV ($\rho = 0$) to 10eV ($\rho = 1$)	Electron temperature	Vector at 6 equidistant ρ locations	Electron Cyclotron Emission or Thomson Scattering
ι	1	0.02	$\sim \rho^{-1}\partial\psi/\partial\rho$	Vector at 6 equidistant ρ locations	Indirectly via Motional Stark Effect

TABLE I

LIST OF PLASMA DIAGNOSTIC SIGNALS (SENSORS) ASSUMED TO BE AVAILABLE FOR THE OBSERVER

D. Nominal case: TCV tokamak plasma ramp-up

We conclude this section by presenting the nominal tokamak plasma simulation used for the remainder of this paper. This simulation is done with the RAPTOR code used in purely predictive mode (i.e. not as a state observer). Parameters for the simulation are chosen so as to be representative of a typical ramp-up in the TCV tokamak [24]. As actuators, the plasma current I_p is used as well as auxiliary heating/current drive sources. The first source deposits additional heat (no current) in the center of the plasma. The second source deposits heat *and* current at $\rho = 0.4$, with a deposition profile defined as Gaussian shapes with a full-width of 0.3.

The inputs (Fig.2(a)) are chosen appropriately to yield $\iota < 1$ everywhere for period of the simulation. The resulting flat ι profile leads to a lower thermal transport (through the shear-dependence explained in Section II-A) and a gradual increase of temperature seen throughout the time-evolution.
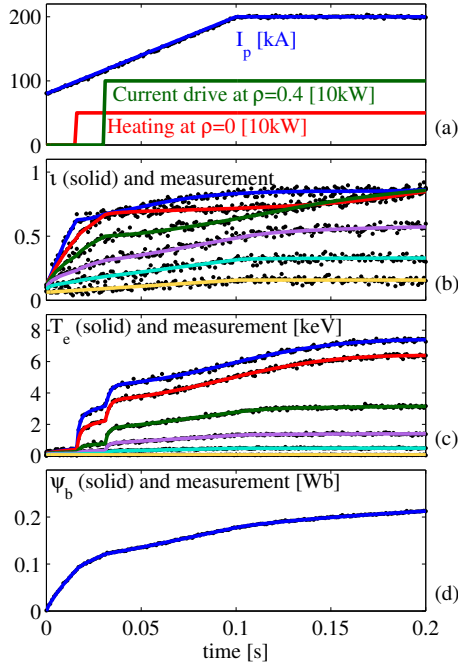

Fig. 2. Nominal simulation of TCV plasma ramp-up with example of (artificial) additive noise. Actuator inputs (and measurement of I_p) are shown in (a). Curves in (b) and (c) represent profile measurements at 6 equidistant points along ρ from $\rho = 0$ to $\rho = 1$, with the highest values obtained in the center. The edge flux and measurement is shown in (d).

III. OBSERVER DESIGN

A. Extended Kalman Filter for estimation of state and disturbances

By defining $f(x_k, u_k)$ as the solution of (11): $\tilde{f}(f(x_k, u_k), x_k, u_k) = 0$ we can compactly write the nonlinear model as:

$$x_{k+1} = f(x_k, u_k), \quad y_k = h(x_k) \tag{17}$$

We assume the output is corrupted by white measurement noise v_k with covariance matrix R_k. The state is subject to process noise w_k^x with covariance matrix Q_k^x. In addition, to-be-estimated disturbances are added to the state equation. These disturbances are modeled as a random walk obeying $d_{k+1} = d_k + w_k^d$ where w_k^d is zero-mean white-noise process with covariance Q_k^d. w_k^d and w_k^x are assumed to be uncorrelated.

The augmented state-space model is written as

$$\begin{bmatrix} x_{k+1} \\ d_{k+1} \end{bmatrix} = \begin{bmatrix} f(x_k, u_k) \\ 0 \end{bmatrix} + \begin{bmatrix} B_k^d \\ I \end{bmatrix} d_k + \begin{bmatrix} w_k^x \\ w_k^d \end{bmatrix} \tag{18}$$

In this case, we choose $B_k^d = I$ such that each state has a corresponding entry in the disturbance vector.

We now define the augmented state

$$z_k = \begin{bmatrix} x_k \\ d_k \end{bmatrix} \in \mathbb{R}^{n_z} \tag{19}$$

and selection matrices $\mathbb{S}_x$ and $\mathbb{S}_d$ such that $x_k = \mathbb{S}_x z_k$, $d_k = \mathbb{S}_d z_k$. Then, defining matrices

$$F_k = \begin{bmatrix} A_k & B_k^d \\ 0 & I_{n_d} \end{bmatrix}, G_k^u = \begin{bmatrix} B_k^u \\ 0 \end{bmatrix}, G_k^w = I_{n_z}, \tag{20}$$

$$H_k = \begin{bmatrix} C_k & 0 \end{bmatrix}, \tag{21}$$

we can write the Extended Kalman Filter equations for the model (18)-(17) (roughly following notation in [12]) as

$$\Omega_k = H_k \Sigma_{k|k-1} H_k^T + R_k \tag{22}$$

$$L_k = \Sigma_{k|k-1} H_k^T \Omega_k^{-1} \tag{23}$$

$$\hat{z}_{k|k} = \hat{z}_{k|k-1} + L_k[y_k - h(\mathbb{S}_x \hat{z}_{k|k-1})] \tag{24}$$

$$\Sigma_{k|k} = (I - \Sigma_{k|k-1} H_k^T \Omega_k^{-1} H_k)\Sigma_{k|k-1} \tag{25}$$

$$\hat{z}_{k+1|k} = \begin{bmatrix} f(\mathbb{S}_x \hat{z}_{k|k}, u_k) + B_k^d d_k \\ d_k \end{bmatrix} + G_k^w w_k \tag{26}$$

$$\Sigma_{k+1|k} = F_k \Sigma_{k|k} F_k^T + G_k^w Q_k G_k^{wT} \tag{27}$$

The above equations evolve $\hat{z}_{k|k}$ and $\Sigma_{k|k}$, respectively the estimates of the augmented state and its covariance matrix. L_k is the Kalman gain. In the filter's numerical implementation, z_k is scaled so that its entries have typical values near

unity. Q_k is the (block-diagonal) covariance matrix of the process noise $w_k = [(w_k^x)^T, (w_k^d)^T]^T$ respectively.

B. Input disturbance determination

An input disturbance u_k^d appears in the linearized state equation as an additional term $B_k^u u_k^d$, therefore an estimate for u_k^d, given an arbitrary disturbance estimate $\hat{d}_k$ can be found by solving the least squares problem $B_k^u \hat{u}_k^d = \hat{d}_k$ with $\hat{d}_k = \mathbb{S}\hat{z}_k$ the disturbance estimate. $\hat{u}_k^d$ is computed from the pseudo-inverse $\hat{u}_d = (B_k^u)^+ \hat{d}_k$ It is expected that a disturbance (or fault) in a single actuator will yield a $\hat{d}_k$ structured so that one term of $\hat{u}_d$ appears out of the noise, while a systematic error (e.g. a modeling error) will appear on multiple input disturbance terms simultaneously. In the simulation examples, this method will be used to estimate input disturbances arising from the variation of the actuator input power.

C. Design of the covariance matrices

In the design of Extended Kalman Filters, a proper choice of the noise covariance matrices is of paramount importance to obtain good results. The measurement covariance matrix can be designed in straightforward fashion by choosing R_k as a diagonal matrix containing the square of the standard deviation of each measurement (as listed in table I) on its diagonal.

We base the design of the state and disturbance noise covariance matrices Q_k^x and Q_k^d on constraints and intuition arising from the physics and numerics of the problem. Since the physical model contains nonlinear coupling via second order spatial derivatives, local variations in the profiles leading to large excursions in the second derivatives can create unphysical situations which lead to numerical divergence. The covariance matrices are therefore designed so as to enforce a high correlation between neighboring spatial points for the simulated physical profiles. Also, since values at the boundary $\rho = 1$ are well-determined from the boundary conditions we expect modeling errors to affect central values (near $\rho = 0$) more than edge values (near $\rho = 1$) of the profiles.

For this purpose, we first design the covariance matrices for the auxiliary vectors $\bar{\psi}$ and $\bar{T}_e$, being the values of ψ respectively T_e on a vector of spatial points $\bar{\rho}$. The covariance matrices for the state and disturbances are defined differently. Starting from the state, first define the covariance $Q_\psi^x = E[\bar{\psi}\bar{\psi}^T]$ and write it as $Q_\psi^x = Q^s \circ Q^\ell$ (where $\circ$ is the element-wise matrix product and Q^s is a symmetric Toeplitz matrix with $\exp(-\bar{\rho}^2/w_s^2)$ (element-wise) as its first row and column, and $Q^\ell = \ell\ell^T$ with $\ell = 0.1 + 0.9(1 - \bar{\rho} \circ \bar{\rho})$. The first matrix enforces spatial smoothing of $\bar{\psi}$, and the second forces the covariance to be lower near the edge. The scalar w_s represents the degree of smoothness, or degree of correlation of neighboring points. The resulting Q_ψ^x is shown in Figure 3(a) Similarly, $Q_{T_e}^x = E[\bar{T}_e\bar{T}_e^T]$ is defined as $Q_{T_e}^x = 10^6 Q_\psi^x$ reflecting the different physical scaling of the two profiles. Noting the linear relation $\bar{\psi} = \bar{\Lambda}_\psi \mathbb{S}_\psi x$ $\bar{T}_e = \bar{\Lambda}_{T_e} \mathbb{S}_{T_e} x$ and

finally defining $\mathbb{L}_\psi = \bar{\Lambda}_\psi \mathbb{S}_\psi$ and $\mathbb{L}_{T_e} = \bar{\Lambda}_{T_e}\mathbb{S}_{T_e}$ the state covariance matrix is written as

$$Q^x = \begin{pmatrix} \mathbb{L}_\psi^+ Q_\psi^x (\mathbb{L}_\psi^T)^+ & 0 \\ 0 & \mathbb{L}_{T_e}^+ Q_x^{T_e}(\mathbb{L}_{T_e}^T)^+ \end{pmatrix} \quad (28)$$

Finally, a time-dependent weighting is applied to the covariance matrix, in order to ensure that the model is weighed more heavily in the first few time steps of the simulation. This is done by multiplying Q^x by a time-dependent term

$$Q_k^x = Q^x(1 - \exp(-20t(k))) \quad (29)$$

The disturbance covariance matrices are defined in identical fashion, but choosing instead $w_s = 0.2$ and $\ell = 1$, reflecting a lower spatial correlation and allowing higher systematic disturbances to the profiles in outer ρ regions. The resulting matrix Q_ψ^d, used to build Q^d in identical fashion as (28), is shown in Figure 3(b)
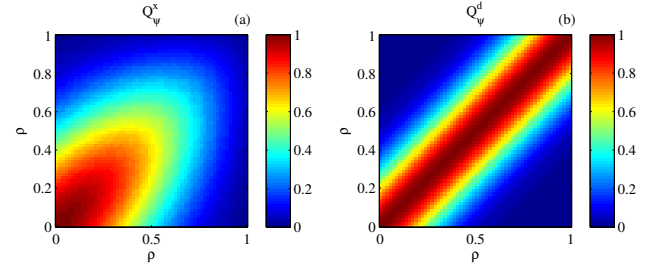

Fig. 3. Profile covariance matrices Q_x^ψ and Q_d^ψ used to construct state and disturbance covariance matrices.

D. Stability and observability

Before proceeding, we briefly mention some stability and observability properties of the system. A full study of the nonlinear stability and observability properties of the system is beyond the scope of this paper. Let us suffice, instead, to study the properties of the time-varying (non-augmented) system around the nominal state trajectory. First of all, we note that thanks to the diffusive nature of the system, A_k is always a stable matrix along physically feasible nominal trajectories. For small deviations from the nominal trajectory, the state reconstruction error $e_k = \hat{z}_k - z_k$ obeys $e_{k+1} = (F_k - L_k H_k)e_k$. Since A_k is stable, so is F_k and for sufficiently small L_k the error is stable. For nonzero L_k, It has been observed that the limiting factor for this algorithm is not so much the risk of destabilizing the observer, but risk of choosing L_k such that the state update causes the state estimate to become unphysical (e.g. negative temperatures), resulting in failure in the nonlinear solver for $x_{k+1} = f(x_k, u_k)$. This is remedied, in practice, by promoting smoothness of the state update through the covariance matrix Q_k as well as ad-hoc fallback strategies to recover from unphysical states.

Furthermore, we investigate the observability properties of the linear time-varying system over an interval $d = n_x$. Defining the time-varying observability matrix $\mathcal{O}_k^d$ [25], we compute the corresponding observability Gramian $\mathcal{G}_k^d =$

$(\mathcal{O}_k^d)^T \mathcal{O}_k^d$ and its SVD $\mathcal{G}_k^d = U_k S_k V_k^T$. The singular values on the diagonal of S_k, for each time k, are plotted in Fig.4(a,b) and show a similar trend for all times. As can be seen, some modes are clearly more observable than others. We then study the time-evolution of the least observable modes by partitioning V_k^T for $k = 1$ in two equal-sized matrices $V_1^T = [(V_1^1)^T, (V_1^2)^T]$ with the most observable modes in V_1^1 and the least observable modes (with singular value < 1) in V_1^2. We then evaluate the time-evolution of these modes. The resulting time-evolutions are plotted in 4(c) and 4(d), for the most and least observable modes, respectively. From the time evolution we can conclude that the least observable modes correspond to those which decay rapidly due to the natural system dynamics. Thus, these modes will not affect the system's time evolution in the long term. Physically, these less-observable modes correspond modes with high spatial frequency which are damped out rapidly by the diffusive nature of the system. Similar analysis starting at other times yields qualitatively similar results. A more systematic study is left as future work, including analyses of robustness vs performance for different noise levels. It should be noted that for the simulations performed for this paper it was possible to obtain satisfactory results with minimal ad-hoc parameter tuning.
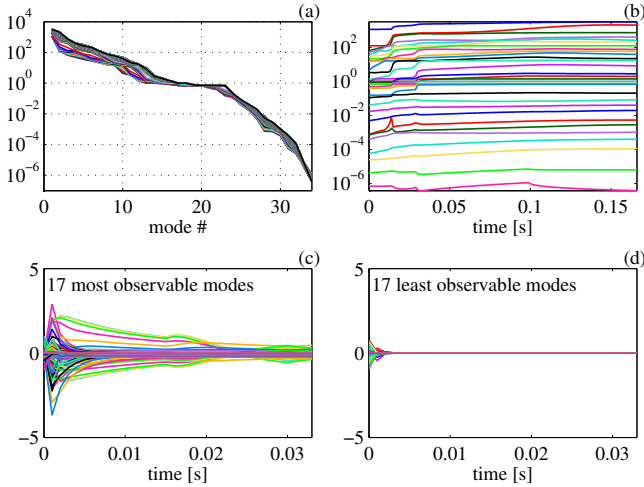

Fig. 4. Observability properties of the (unaugmented) system. Singular values of the observability Gramian (a) and their time evolution (b). The time evolution of well-observable (c) vs. non-well-observable (d) modes shows that less observable modes decay very rapidly.

IV. SIMULATION RESULTS

A. Implementation and performance metrics

The observer is implemented in MATLAB®. Simulations shown in this paper, for 34 states and 34 disturbances (yielding 68 elements for the augmented state) take comparable time as a forward simulation, since the matrix equations required for the Kalman Filter are a much smaller computational burden than solving the nonlinear problem for a time step update. To obtain deterministic computational times, the maximum number of Newton iterations is fixed at to 3, which is sufficient to obtain a converged solution after only a few time steps.

The EKF-based observer returns the state and disturbance estimates as well as their covariance matrices. Also, the innovation sequence $y_k - h(\mathbb{S}_x \hat{z}_{k|k-1})$ can be monitored to assess the filter's performance. If the underlying system is linear, the innovation sequence is theoretically expected to be a zero-mean white noise sequence, and even for the nonlinear system at hand the whiteness of the innovation sequence is expected to give an indication of the quality of the filter estimates. The innovation sequence will also be used to determine and isolate sensor faults in future studies.

B. Simulation results

1) State estimation for nominal model model: We first show, in Figure 5, the filter output for the nominal disturbance-free case of Fig.2. The filter estimates are shown to correctly track the true states and error bars display the standard deviation calculated from the covariance matrix diagonals. As can be expected for this disturbance-free case, the estimated disturbances are close to zero. The innovation sequence is also zero-mean. The estimated input disturbances are also close to zero as expected.

2) Identification of input disturbances: In the next example, we demonstrate the filter's capability of determining input disturbances. In this simulation, disturbances were applied for a short period to the two power actuators. The disturbances, together with their estimates, are shown in Fig.6(e). After some time, the disturbances converge to stationary values corresponding to the injected (unknown) disturbance. When the input disturbance is removed, the disturbance estimates converge to zero again. The speed of convergence can be tuned by scaling the covariance matrix Q_k^d. Note that the disturbance states Fig.6(c) start to deviate from zero as soon as the disturbance is injected, causing the innovation sequence Fig.6(d) to deviate from zero-mean indicating a systematic discrepancy between estimated and predicted measurements. Once the disturbances estimates converge to a stationary value, the innovation sequence mean returns to 0 indicating the measurement outputs no longer contains systematic offsets from the modeled measurements. The states are correctly estimated despite the disturbances, as is visible in Fig.6(a,b).

3) Response to perturbed model parameters: As a final example, we illustrate the effect of a systematic (modeling) error on the observer. We increase the thermal conductivity by 30% and test the observer designed for the nominal model on the new data. The results, shown in Fig.7 show that the observer still tracks the state correctly, but that a systematic disturbance appears which settles to a stationary value after some time. The shape of this disturbance, in terms of the physical profiles, is shown in Figure 8. This is shown as the profiles of ψ and T_e corresponding to the steady-state disturbance term, computed from spline basis coefficients $\hat{\psi}_d = \mathbb{S}_\psi \hat{d}$ and $\hat{\mathbf{T}}_\mathbf{e} = \mathbb{S}_{T_e} \hat{d}$ using (4),(5). Note that the ψ profile disturbance is very small (measured in mWb) and while there is a significant T_e profile disturbance.
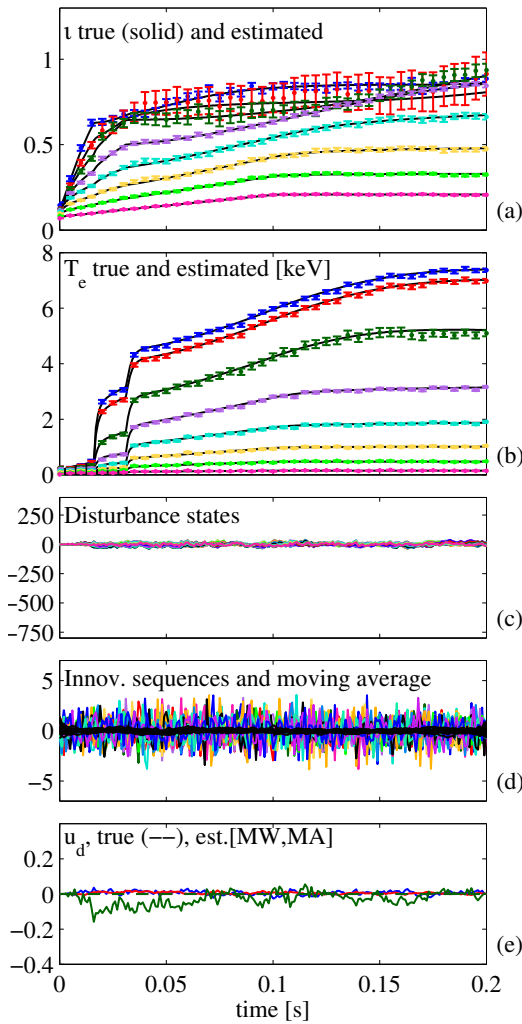
ι true (solid) and estimated

1

0.5

0

(a)

T_e true and estimated [keV]

8
6
4
2
0

(b)

Disturbance states

250
0
−250
−500
−750

(c)

Innov. sequences and moving average

5
0
−5

(d)

u_d, true (−−), est.[MW,MA]

0.2
0
−0.2
−0.4

(e)

0   0.05   0.1   0.15   0.2
time [s]

ι true (solid) and estimated

1

0.5

0

(a)

T_e true and estimated [keV]

8
6
4
2
0

(b)

Disturbance states

250
0
−250
−500
−750

(c)

Innov. sequences and moving average

5
0
−5

(d)

u_d, true (−−), est.[MW,MA]

0.2
0
−0.2
−0.4

(e)

0   0.05   0.1   0.15   0.2
time [s]

Fig. 5. Output of the observer for the nominal case (also shown in Fig.2). State estimate results are shown (a), (b) together with errorbars representing the square root of the covariance matrix diagonals. Disturbance states (c) and the resulting estimated input disturbances (e) remain close to zero in this nominal (disturbance-free) case. The innovation sequence and its 20-point moving average (d) are also shown.
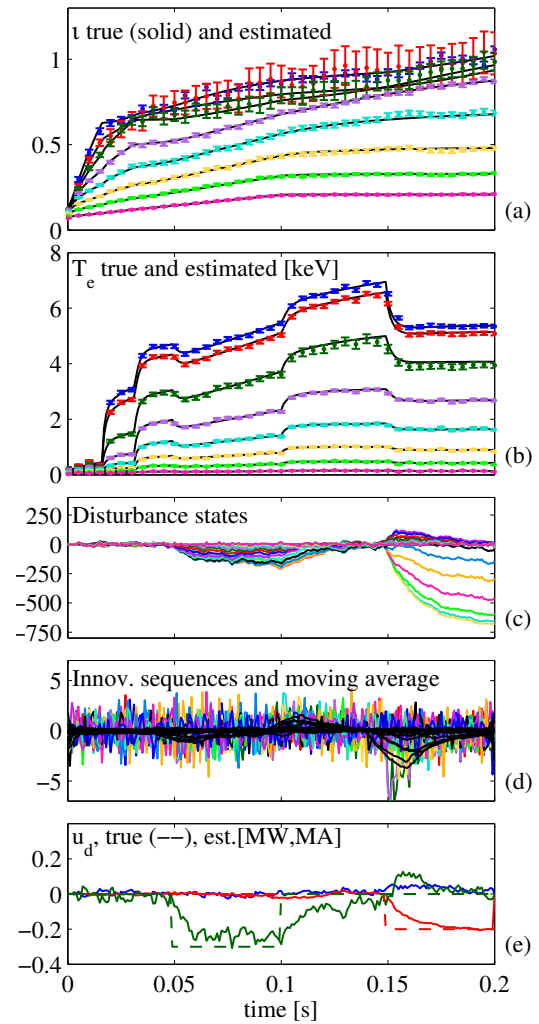
Fig. 6. Observer results in simulation with artificial input disturbances in the power of the auxiliary heating systems. The observer correctly estimates the disturbances and determines the corresponding disturbed input after a short time.

This can be understood by realizing that the higher thermal transport leads to, effectively, a lower temperature than the observer model expects. This is accounted for in the observer by introducing a negative temperature profile disturbance. Contrary to the previous case, the disturbance does not have the structure associated with one particular input, thus this disturbance can not be classified as an input disturbance but as a structural disturbance arising from a modeling error. The fact the innovation sequence eventually becomes zero-mean indicates that the disturbance estimates successfully remove the systematic difference between estimated and measured outputs.

V. CONCLUSIONS

This paper has introduced a model-based state observer for the coupled dynamics of the internal profiles of a tokamak plasma. The observer is based on an Extended Kalman Filter which estimates an augmented state consisting of physical states and random-walk disturbances. The physical model of the plant is derived from a spatially discretized PDE, yielding a nonlinear set of ODEs for which the derivatives are evaluated analytically by the RAPTOR code. Model parameters are chosen constant in this work and modeling errors are absorbed by the disturbance estimates. These disturbances are compared to the expected signature of input disturbances to determine whether the disturbance can be attributed to an input disturbance or to a different problem. Simulation results show the effectiveness of the proposed approach.

Further work is possible in the analysis of observability of the system along more general trajectories than the specific one studied here. Also, more systematic classification of disturbances can be developed. Sensor faults can also be detected via the innovation sequence and the whole observer can be embedded in a more comprehensive residual-based fault detection scheme. Future studies will also aim at testing this approach on simulation data from more com-
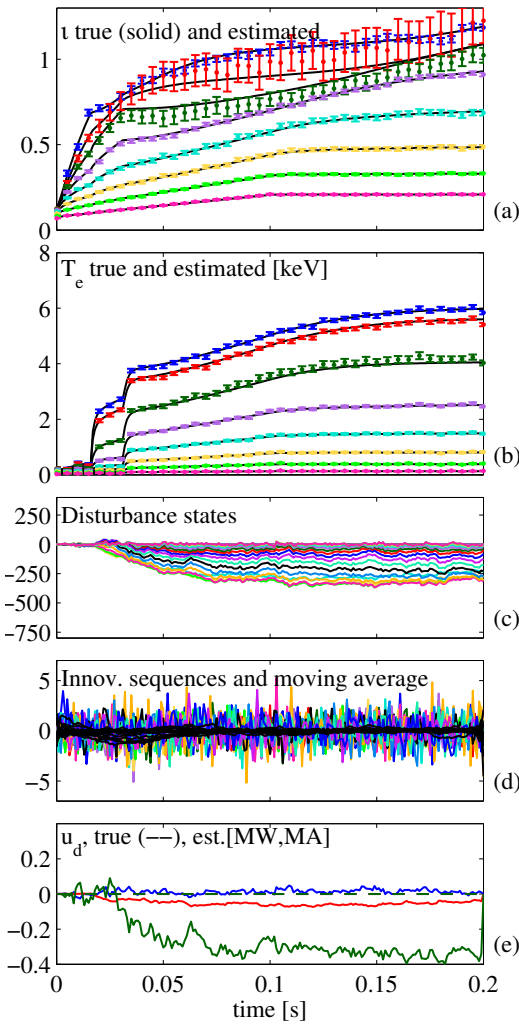
Fig. 7. Observer results for a perturbed model with 30% higher thermal conductivity than the nominal model used for designing the observer. The observer estimates a systematic disturbance to compensate for the modeling errors.
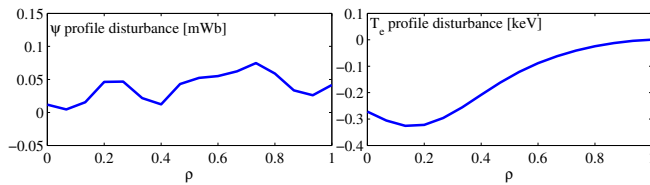

Fig. 8. Physical profiles corresponding to steady-state estimated disturbance $\hat{d}_k$ for the simulation shown in Figure 7.

plete physics-based transport codes, in order to validate the validity modeling assumptions in this context. Investigations of reduced-order observers can also be undertaken to yield simpler and computationally more attractive solutions. Tests on actual diagnostic data are also underway as this algorithm is deployed to existing tokamaks, and will require more complex sensor models. Finally, the proposed observer is to be tested in closed-loop feedback control schemes, for which controllers can be designed to take the estimated disturbances into account.

[1] A. Pironti and M. Walker, "Control of tokamak plasmas: introduction to a special section," *Control Systems, IEEE*, vol. 25, no. 5, pp. 24 – 29, oct. 2005.

[2] ——, "Control of tokamak plasmas. ii," *Control Systems, IEEE*, vol. 26, no. 2, pp. 30 – 31, april 2006.

[3] A. Donné, *et al.*, "Chapter 7: Diagnostics," *Nuclear Fusion*, vol. 47, no. 6, p. S337, 2007. [Online]. Available: http://stacks.iop.org/0029-5515/47/i=6/a=S07

[4] J. Ferron, *et al.*, "Real time equilibrium reconstruction for tokamak discharge control," *Nuclear Fusion*, vol. 38, no. 7, p. 1055, 1998.

[5] J. Blum, C. Boulbe, and B. Faugeras, "Real-time plasma equilibrium reconstruction in a tokamak," *Journal of Physics: Conference Series*, vol. 135, no. 1, p. 012019, 2008.

[6] D. Moreau, *et al.*, "A two-time-scale dynamic-model approach for magnetic and kinetic profile control in advanced tokamak scenarios on jet," *Nuclear Fusion*, vol. 48, no. 10, p. 106001, 2008.

[7] Y. Ou, *et al.*, "Optimal tracking control of current profile in tokamaks," *Control Systems Technology, IEEE Transactions on*, vol. 19, no. 2, pp. 432 –441, march 2011.

[8] J. E. Barton, *et al.*, "Toroidal current profile control during low confinement mode plasma discharges in DIII-D via first-principles-driven model-based robust control synthesis," *Nuclear Fusion*, vol. 52, no. 12, p. 123018, 2012. [Online]. Available: http://stacks.iop.org/0029-5515/52/i=12/a=123018

[9] F. B. Argomedo, *et al.*, "Lyapunov-based distributed control of the safety-factor profile in a tokamak plasma," *Nuclear Fusion*, vol. 53, no. 3, p. 033005, 2013. [Online]. Available: http://stacks.iop.org/0029-5515/53/i=3/a=033005

[10] C. Xu, Y. Ou, and E. Schuster, "Transport parameter estimations of plasma transport dynamics using the extended kalman filter," *Plasma Science, IEEE Transactions on*, vol. 38, no. 3, pp. 359 –364, March 2010.

[11] S. Mechhoud, *et al.*, "Combined distributed parameters and source estimation in tokamak plasma heat transport," in *European Control Conference*, 2012.

[12] B. Anderson and J. Moore, *Optimal filtering*. Mineola, NY (USA): Dover Publications, 1979.

[13] F. Felici, *et al.*, "Real-time physics-model-based simulation of the current density profile in tokamak plasmas," *Nuclear Fusion*, vol. 51, no. 8, p. 083052, 2011.

[14] F. Felici and O. Sauter, "Non-linear model-based optimization of actuator trajectories for tokamak plasma profile control," *Plasma Physics and Controlled Fusion*, vol. 54, no. 2, p. 025002, 2012.

[15] F. L. Hinton and R. D. Hazeltine, "Theory of plasma transport in toroidal confinement systems," *Rev. Mod. Phys.*, vol. 48, no. 2, pp. 239–308, April 1976.

[16] G. V. Pereverzev and P. Yushmanov, "ASTRA Automated System for TRansport Analysis in a Tokamak," IPP Report, Tech. Rep. 5/98, February 2002.

[17] S. H. Kim, *et al.*, "Full tokamak discharge simulation of ITER by combining DINA-CH and CRONOS," *Plasma Physics and Controlled Fusion*, vol. 51, no. 10, pp. 105 007–+, Oct. 2009.

[18] J. Artaud, *et al.*, "The CRONOS suite of codes for integrated tokamak modelling," *Nuclear Fusion*, vol. 50, no. 4, p. 043001, 2010.

[19] E. Witrant, *et al.*, "A control-oriented model of the current profile in tokamak plasma," *Plasma Physics and Controlled Fusion*, vol. 49, no. 7, pp. 1075–1105, 2007.

[20] C. Xu, *et al.*, "Ramp-up-phase current-profile control of tokamak plasmas via nonlinear programming," *Plasma Science, IEEE Transactions on*, vol. 38, no. 2, pp. 163 –173, February 2010.

[21] Y. Ou, C. Xu, and E. Schuster, "Robust control design for the poloidal magnetic flux profile evolution in the presence of model uncertainties," *Plasma Science, IEEE Transactions on*, vol. 38, no. 3, pp. 375 –382, March 2010.

[22] F. Felici, "Real-Time Control of Tokamak Plasmas: from Control of Physics to Physics-Based Control," Ph.D. dissertation, Ecole Polytechnique Fédérale de Lausanne EPFL, Lausanne, 2011.

[23] C. de Boor, *A Practical Guide to Splines*, ser. Applied Mathematical Science. Springer-Verlag, New York, 2001, vol. 27.

[24] F. Hofmann, *et al.*, "Creation and control of variably shaped plasmas in TCV," *Plasma Physics and Controlled Fusion*, vol. 36, no. 12B, p. B277, 1994.

[25] W. J. Rugh, *Linear Systems Theory*, 2nd ed. Upper Saddle River, New Jersey: Prentice-Hall, 1996, iSBN: 0-13-441205-2.